Research Square

Preprints are preliminary reports that have not undergone peer review.
They should not be considered conclusive, used to inform clinical practice,
or referenced by the media as validated information.

Electrically Controlled Ultrawideband THz Spatial Light Modulator for Hyperspectral and Three-Dimensional Single-Pixel Imaging

Yiwen Sun

775319806@qq.com

Key Laboratory of Optoelectronic Devices and Systems of Ministry of Education and Guangdong Province, College of Physics and Optoelectronics Engineering,

Xudong Liu

Department of Biomedical Engineering, School of Medicine, Shenzhen University

Wenjing Ma

Shenzhen University

Chenyu Wang

Department of Biomedical Engineering, School of Medicine,

Chuanfu Sun

Department of Biomedical Engineering, School of Medicine, Shenzhen University

Yu Liao

Department of Biomedical Engineering, School of Medicine,

Emma Pickwell-MacPherson

University of Warwick https://orcid.org/0000-0001-6062-5959

Songlin Zhuang

University of Shanghai for Science and Technology

Xiaoyu Weng

Shenzhen University https://orcid.org/0000-0001-9654-3517

Junle Qu

Shenzhen University https://orcid.org/0000-0001-7833-4711

Article

Keywords:

Posted Date: August 5th, 2026

DOI: https://doi.org/10.21203/rs.3.rs-10453315/v1

License: This work is licensed under a Creative Commons Attribution 4.0 International License.
Read Full License

Additional Declarations: There is no conflict of interest

Electrically Controlled Ultrawideband THz Spatial Light Modulator for Hyperspectral and Three-Dimensional Single-Pixel Imaging

Xudong Liu[1], Wenjing Ma[2], Chenyu Wang[3], Chuanfu Sun[3], Yu Liao[3], Emma Pickwell-MacPherson[4], Songlin Zhuang[5], Xiaoyu Weng[1¶], Junle Qu[1#], Yiwen Sun[1*]

[1]Key Laboratory of Optoelectronic Devices and Systems of Ministry of Education and Guangdong Province, College of Physics and Optoelectronics Engineering, Shenzhen University, Shenzhen, 518060, China

[2]National Engineering Laboratory for Big Data System Computing Technology, Shenzhen University, Shenzhen 518060, China

[3]Department of Biomedical Engineering, School of Medicine, Shenzhen University, Shenzhen 518060, China

[4]Department of Physics, University of Warwick, Coventry CV4 7AL, United Kingdom

[5]School of Optical-Electrical and Computer Engineering, University of Shanghai for Science and Technology, Shanghai, China

¶xiaoyu@szu.edu.cn, #jlqu@szu.edu.cn, *ywsun@szu.edu.cn

Abstract:

Terahertz time-domain spectroscopy imaging inherently encodes both spectral and depth information within the temporal profile of each pulse, which makes it attractive for non-destructive evaluation. However, the implementation of electrically programmable single-pixel imaging in the THz range has been hindered by the narrowband or discrete-frequency nature of most existing spatial light modulators, leading to a trade-off between modulation flexibility and the preservation of broadband waveform information. Here, we demonstrate an electrically controlled ultrawideband THz spatial light modulator based on a non-resonant GaAs Schottky microslit array, enabling hyperspectral and three-dimensional single-pixel imaging over an ultrawideband spectral range from 0.2 to 1.4 THz. With a 64-pixel effective Hadamard aperture and a Diag-ordered sampling sequence, the system enables hyperspectral spectral-fingerprint imaging, transmission- and reflection-mode three-dimensional reconstruction, and dynamic imaging with a frame acquisition time of approximately 9 s. This work establishes a waveform-preserving, electronically reconfigurable encoding platform that provides a compact solution for multidimensional THz imaging, with potential use in pharmaceutical screening, industrial inspection, biomedical diagnosis, and security screening.

Introduction

Terahertz time-domain spectroscopy (THz-TDS) captures the full temporal electric field of broadband THz pulses, enabling simultaneous extraction of frequency-dependent spectral fingerprints, phase-sensitive optical responses, and time-of-flight depth information from a single waveform. These attributes render THz-TDS attractive for applications ranging from nondestructive evaluation and multilayer structure

inspection to chemical sensing, pharmaceutical analysis, biomedical diagnostics, and cultural heritage preservation[1-7]. Conventional THz-TDS imaging, however, relies on point-by-point raster scanning, which incurs long acquisition times and increased system complexity. Plasmonic photoconductive focal-plane arrays have recently circumvented this limitation by enabling direct spatial, temporal, and spectral capture without mechanical scanning[8], yet their reliance on specialized array detectors and readout electronics distinguishes them from compact single-detector architectures based on spatial encoding.

Single-pixel imaging addresses this gap by shifting the spatial sampling burden from detector arrays to programmable spatial modulators[9]. In this framework, the modulator dictates the usable bandwidth, modulation efficiency, system compactness, and, critically, whether the coherent THz-TDS waveform remains intact during encoding. Optically controlled modulation schemes, such as DMD-patterned visible illumination on silicon, have achieved real-time THz video acquisition while preserving time-resolving capability[1,6,10], but they require additional patterning optics and photoexcited modulation planes, motivating the pursuit of directly electrically addressed alternatives.

Recent electrically programmable THz spatial modulators have made substantial progress. Reconfigurable intelligent surfaces offer programmable wavefront control at 100 GHz[11]. Liquid-crystal transmissive metasurfaces enable compact compressive imaging near 0.44–0.45 THz[12]. Broadband liquid-crystal THz spatial light modulators have extended electrically controlled operation to 0.2-1.0 THz for multispectral imaging and beam scanning[13]. Despite these advances, a directly electrically addressed, compact in-line THz spatial encoder that preserves coherent THz-TDS waveforms over a broad continuous bandwidth for simultaneous hyperspectral and time-of-flight imaging has remained elusive.

Here, we introduce a non-resonant GaAs Schottky microslit THz spatial light modulator that enables electrically controlled ultrawideband single-pixel imaging from 0.2 to 1.4 THz. The device preserves the complete coherent THz-TDS waveform for each spatial mask, functioning as a broadband encoder that supports both hyperspectral reconstruction and time-of-flight depth discrimination within a single measurement sequence. Combined with a Diag-ordered Hadamard sampling strategy, the system provides a robust acquisition workflow under practical THz imaging conditions, including limited modulation depth, nonuniform illumination, and reduced post-sample

signal-to-noise ratio. We validate this platform through hyperspectral spectral-fingerprint imaging, three-dimensional reconstruction in both transmission and reflection geometries, and dynamic imaging with a frame acquisition time of approximately 9 s. This work establishes an electrically programmable, waveform-preserving THz spatial encoding platform for multidimensional single-pixel imaging, with potential applicability in pharmaceutical screening, industrial inspection, biomedical diagnostics, and security screening.

Results

1. Principle of electrically encoded THz single-pixel imaging framework

1.1. System architecture and dual-domain imaging principle

Figure 1 illustrates an electrically encoded ultrawideband THz single-pixel imaging system based on a GaAs Schottky microslit spatial light modulator. A broadband THz pulse is first spatially encoded by the programmable THz-SLM, then transmitted through the sample, and finally collected by a single photoconductive detector. For every displayed mask, the complete temporal electric-field waveform is retained, allowing one acquisition framework to carry both spectral and depth information.

The retained waveform serves two complementary imaging functions. In the frequency domain, selected spectral components are used to reconstruct spatial images and form an *x*–*y*–frequency hyperspectral data cube, as shown in Figure 1b. In the time domain, selected temporal delays are used to reconstruct depth-resolved slices associated with different optical paths or internal interfaces, as illustrated in Figure 1c. Thus, the same waveform that reveals spectral fingerprints also resolves structural depth, distinguishing the proposed system from intensity-only single-pixel imaging.

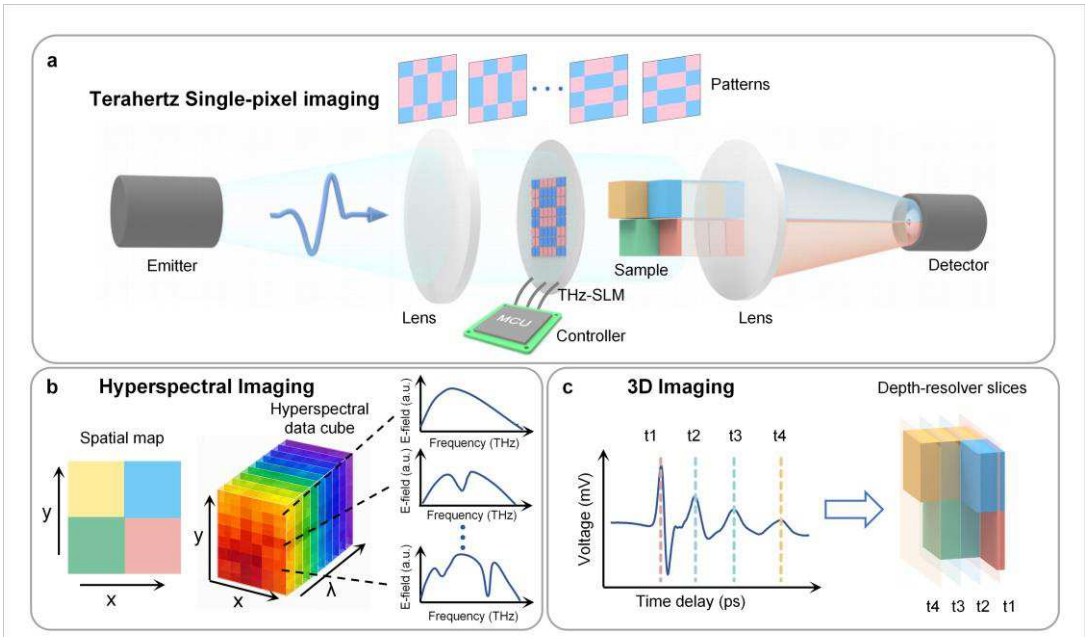


Figure 1. Electrically controlled THz single-pixel imaging for hyperspectral and three-dimensional (3D) reconstruction. a, Schematic of the proposed system, where a broadband THz pulse is spatially encoded by an electrically addressed THz-SLM and detected by a single-pixel detector after interaction with a sample featuring height variations and region-dependent THz absorption. **b**, Hyperspectral imaging principle. The full THz waveform is used to construct a hyperspectral data cube in x, y, and λ; the three spectra on the right schematically denote the THz frequency-domain responses from different sample regions in the x–y plane. **c**, Time-of-flight 3D imaging principle. Different temporal delays (t_1–t_4) correspond to different depth-resolved slices for three-dimensional reconstruction.

1.2. Modulation mechanism and performance of the electrical THz-SLM

To realize this waveform-preserving spatial encoding, we developed an electrically controlled THz-SLM based on GaAs Schottky microslits. As shown in Figure 2a-c, the device comprises a 10 × 10 array of independently addressable pixels integrated on a printed circuit board, providing an active modulation area of 34×34 mm². The array is formed on a lightly doped *n*-GaAs layer grown on a semi-insulating GaAs substrate, with a measured carrier concentration of 2×10^{17} cm^{-3}. This carrier concentration provides sufficient absorption in the unbiased state while still allowing efficient depletion under reverse bias.

Each 3×3 mm² pixel contains subwavelength gold microslits forming a Schottky contact with the *n*-GaAs layer, together with an adjacent Ohmic contact for electrical biasing. The microslit period is 8 μm and the slit width is 2 μm. The current-voltage

response of a representative pixel exhibits clear Schottky rectification (Supplementary Fig. S14), confirming the electrical junction required for bias-controlled carrier depletion.

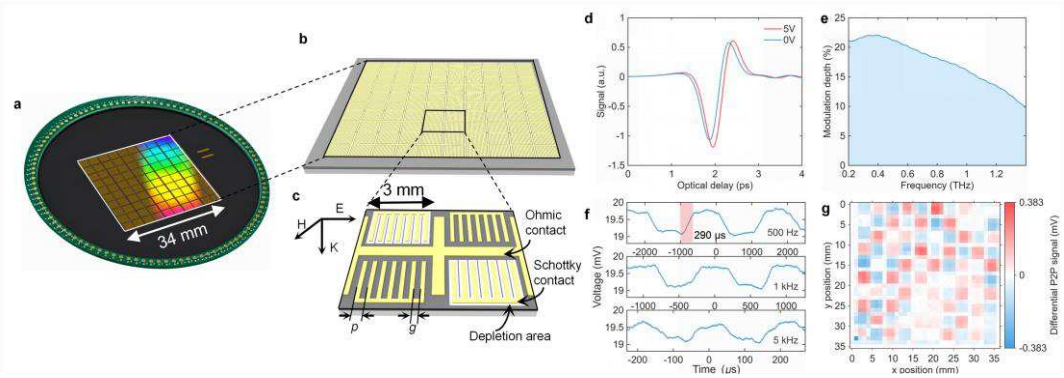


Figure 2. Electrically controlled ultrawideband THz-SLM: device architecture and performance. a, Photograph of the fabricated 10 × 10 THz-SLM chip wire-bonded to a printed circuit board (PCB), with a total active area of 34 × 34 mm². **b,** Schematic of the full modulation array. **c,** Enlarged view of a unit pixel composed of Schottky microslits and an Ohmic contact with each pixel measuring 3 × 3 mm². Reverse bias induces a depletion region beneath the Schottky contact, thereby reducing free-carrier absorption and modulating THz transmission. The incident THz field is polarized perpendicular to the microslits; *p* and *g* denote the microslit period and slit width, respectively. **d,** Time-domain THz waveforms measured from a selected pixel at 0 V and 5 V. **e,** Broadband modulation depth spectrum measured from a selected pixel. **f,** Switching response of the full 10 × 10 THz-SLM measured at 500 Hz, 1 kHz, and 5 kHz, with an extracted rise time of about 290 µs. **g,** Spatial distribution of the differential peak-to-peak THz signal over the modulator area.

The modulation mechanism relies on the synergistic effect of carrier depletion and field confinement. When the incident THz polarization is perpendicular to the microslits, the field is confined within the narrow gaps, producing broadband non-resonant enhancement that overlaps strongly with the electrically controlled carrier region beneath the Schottky contact[14,15]. At 0 V, free carriers absorb the incident THz field, yielding a low-transmission state (element "0"). Under reverse bias, the depleted carrier region expands, free-carrier absorption decreases, and the pixel switches to a high-transmission state (element "1"). Because this transition is governed by carrier-density modulation and non-resonant confinement rather than resonance shifting, the modulation remains broadband across the THz-TDS spectral window.

This broadband response was verified experimentally using a focused THz beam. Figure 2d shows the time-domain waveforms measured from a representative pixel at 0 V and 5 V, with the reverse-biased state exhibiting higher THz transmission. The same waveforms were then transformed into the frequency domain, revealing continuous modulation from 0.2 to 1.4 THz, as shown in Figure 2e. The intensity-domain modulation depth is defined as

$$MD = \left(1 - E_{0V}^2 \,/\, E_{5V}^2\right) \times 100\%, \tag{1}$$

where E_{0V} and E_{5V} denote the Fourier-domain field amplitudes measured at 0 V and 5 V reverse bias, respectively. The modulation depth exceeds 20% from 0.2 to 0.6 THz and gradually decreases at higher frequencies. This decrease follows the Drude response of free carriers in n-GaAs: as the carrier conductivity and absorption weaken with increasing frequency, the transmission contrast between the undepleted and depleted states is correspondingly reduced[16].

We further evaluated the temporal response of the THz-SLM by synchronously switching the full 10×10 array between all-off and all-on states under square-wave driving. As shown in Figure 2f, the device follows modulation frequencies of 500 Hz, 1 kHz, and 5 kHz, with an extracted rise time of approximately 290 μs. This value, which reflects practical array-level driving conditions including capacitive loading and interconnect effects, represents a conservative estimate of the system-level response. With this kilohertz-scale switching capability, the device is sufficiently fast for our imaging experiments, whose acquisition time is primarily governed by THz-TDS waveform recording, lock-in detection, and the number of projected masks.

Having established the temporal response, we next examined the spatial encoding performance of the SLM. As shown in Figure 2g, the differential peak-to-peak THz response measured across the active area reveals a clear pixelated distribution, confirming that the array can function as an electrically programmable spatial encoder. Frequency-dependent modulation-depth maps are provided in Supplementary Fig. S4. For Hadamard single-pixel imaging, we selected an 8 × 8 subarray from the 10 × 10 device to satisfy the power-of-two requirement while excluding non-functional pixels.

Each ±1 Hadamard basis was implemented using a binary mask and its complement, and the difference between the two measured signals provided the corresponding effective Hadamard coefficient. This complementary encoding scheme effectively suppresses common-mode fluctuations and provides a robust foundation for compressed THz single-pixel reconstruction.

1.3. Diag-ordered Hadamard sampling

To further enhance reconstruction robustness under practical THz imaging conditions, which often suffer from limited modulation depth, nonuniform illumination, and reduced post-sample signal-to-noise ratio, we developed a Diag-ordered Hadamard sampling strategy. This ordering addresses the inherent vulnerability of high-sequency measurements to noise by arranging Hadamard coefficients in a two-dimensional sequency domain and sampling them along progressively expanding diagonal paths (Figure 3). For an $L \times L$ image, let m and n denote the horizontal and vertical sequency indices in the two-dimensional Walsh–Hadamard domain. Diag acquires the coefficients according to progressively increasing antidiagonal index $m + n$. After scanning to the q-th antidiagonal, the set of acquired coefficients is defined as

$$\Omega_q = \{(m,n) |\ m+n \le q, 0 \le m,n < L\}. \tag{2}$$

As q increases, the sampled region expands from the low-sequency corner toward higher sequencies in both spatial directions. Early measurements therefore preferentially capture coefficients associated with the global structure of the object, while subsequent measurements progressively recover edges and finer details. For a sampling set Ω containing M coefficients, an effective average measurement signal-to-noise ratio can be expressed as

$$SNR_{eff} = \frac{\Sigma \left| C_{m,n} \right|^2}{M \sigma^2}, \tag{3}$$

where $C_{m,n}$ denotes the Hadamard coefficient and σ^2 is the noise variance of each complementary differential measurement. At the same sampling ratio and noise level,

the early acquisition of high-energy low-sequency coefficients increases the effective measurement SNR and supports more stable undersampled reconstruction. Compared with Paley[10], Walsh[17], and Cake-Cutting[18] orderings, Diag combines a balanced two-dimensional sequency progression with a simple deterministic rule for scalable mask generation.

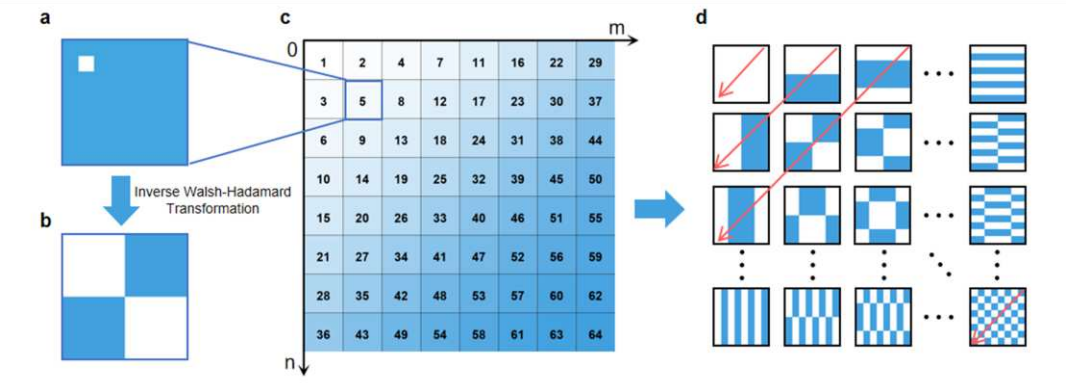


Figure 3. Construction of the proposed Diag-ordered Hadamard sampling strategy. a, Schematic of a two-dimensional Dirac-like sequency map with a single non-zero element. **b,** Corresponding spatial encoding pattern obtained by inverse Walsh-Hadamard transformation, where the non-zero coefficient in the sequency domain is mapped into a spatial Hadamard basis pattern with alternating +1 and −1 values; in experiments, these are implemented using complementary binary 0/1 masks. **c,** Diag ordering matrix in the two-dimensional sequency domain. The numbers indicate the sampling order of coefficients along progressively expanding diagonal paths, while *m* and *n* denote the sequency indices in the horizontal and vertical directions, respectively. **d,** Representative spatial Hadamard encoding patterns generated from the Diag sequence, illustrating the gradual progression from low-sequency to high-sequency components.

In our experiment, each ±1 Hadamard pattern was implemented by sequentially displaying a binary mask and its complementary inverse mask on the THz-SLM. The differential signal between the two measurements was used as the effective Hadamard coefficient, and the resulting measurement vectors were reconstructed using augmented Lagrangian and alternating direction algorithm (TVAL3)[19]. Detailed algorithm construction, comparisons with other Hadamard orderings, and numerical evaluations are provided in the Supplementary Information. This complementary Diag-ordered acquisition provides a simple and deterministic sampling workflow for robust hyperspectral and time-of-flight THz single-pixel reconstruction.

2. Hyperspectral THz spectral-fingerprint imaging

2.1. Broadband frequency-resolved reconstruction

With the hardware and sampling strategy in place, we first validated frequency-resolved THz single-pixel imaging using a metallic aperture target. In this experiment, the focused-beam raster-scanning setup used for SLM characterization was replaced by the collimated imaging configuration shown in Figure 1. The collimated THz beam was spatially encoded by the electrically controlled SLM, transmitted through the sample, and collected by a single detector. The microcontroller unit (MCU) sequentially displayed Diag-ordered Hadamard masks on the binary SLM. Each mask was paired with its complement, and the difference between the two measured responses provided an effective ±1 Hadamard coefficient to improve the signal-to-noise ratio. Because a complete temporal waveform was recorded for every mask, the same measurements

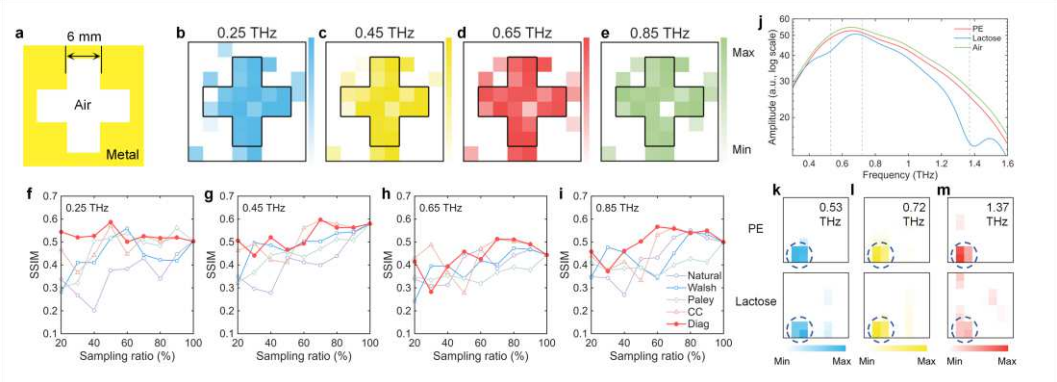


Figure 4. Frequency-resolved and spectral-fingerprint THz single-pixel imaging. a, Schematic of the metallic aperture sample used for frequency-resolved imaging. The sample consists of a metal plate with a cross-shaped air aperture, with a characteristic aperture width of 6 mm. **b–e,** Reconstructed THz single-pixel images of the metallic aperture at 0.25 THz, 0.45 THz, 0.65 THz, and 0.85 THz, respectively, obtained using the Diag-ordered Hadamard sampling strategy. The black outlines indicate the designed aperture geometry. **f–i,** Structural similarity index measure (SSIM) of reconstructed images as a function of sampling ratio at 0.25 THz, 0.45 THz, 0.65 THz, and 0.85 THz, respectively. The proposed Diag ordering is compared with Natural, Walsh, Paley, and Cake-Cutting orderings. **j,** Measured THz transmission spectra of polyethylene (PE), α-lactose monohydrate, and air, showing the characteristic spectral contrast between PE and α-lactose monohydrate. **k–m,** Spectral-fingerprint THz single-pixel images of PE and α-lactose monohydrate tablets reconstructed at 0.53 THz, 0.72 THz, and 1.37 THz, respectively. The dashed circles mark the same regions of interest across different frequencies, confirming that the image contrast follows the material-dependent THz spectral response rather than fixed spatial nonuniformity.

could be Fourier transformed to reconstruct spatial images at selected frequencies across the effective bandwidth.

Figure 4a shows the metallic target, consisting of a cross-shaped air aperture with a characteristic width of 6 mm. The reconstructed images at 0.25, 0.45, 0.65, and 0.85 THz are shown in Figure 4b-e. The aperture is resolved at all four frequencies using a sampling ratio of 70%, confirming that the SLM preserves broadband spectral information during spatial encoding and supports frequency-resolved image reconstruction.

2.2. Algorithmic comparison

Having established broadband reconstruction, we next compared the influence of different Hadamard ordering strategies on image quality. Figure 4f-i present the structural similarity index measure (SSIM) obtained with Paley[10], Natural[17], Walsh[17], Cake-Cutting[18], and Diag orderings at the same four frequencies and across different sampling ratios. Diag provides stable reconstruction performance over a broad range of frequencies and sampling conditions, consistent with its balanced progression from low- to high-sequency components. This stability is particularly useful in practical THz imaging, where limited modulation depth, nonuniform illumination, and post-sample noise can weaken the recovery of fine spatial details.

2.3. Spectral-fingerprint material contrast

Building on this structural imaging capability, we extended the broadband reconstruction to spectral-fingerprint-based material discrimination. α-lactose monohydrate exhibits characteristic absorption features near 0.53 THz and 1.37 THz[20], polyethylene (PE) has a comparatively smooth transmission response over the same range[21]. To identify suitable imaging frequencies, reference spectra of α-lactose monohydrate, PE, and air were first measured using a conventional THz-TDS transmission setup. As shown in Figure 4j, the lactose spectrum contains clear transmission minima near 0.53 and 1.37 THz, while PE remains relatively transmissive, providing the spectral basis for material-selective reconstruction.

We subsequently reconstructed hyperspectral single-pixel images at 0.53, 0.72, and 1.37 THz (Figures 4k-m). The frequencies at 0.53 and 1.37 THz probe the characteristic absorption bands of α-lactose monohydrate, while 0.72 THz serves as a reference. The reconstructed images exhibit clear frequency-dependent material contrast. PE maintains relatively high transmission at all three frequencies, while the lactose response decreases at the absorption frequencies. The dashed circles mark identical regions of interest across the reconstructed images, allowing the frequency-dependent contrast to be compared at fixed spatial positions. This comparison reduces the influence of illumination nonuniformity, pixel-to-pixel modulation variation, and fixed reconstruction artifacts, indicating that the observed contrast originates primarily from the material spectra. These results thus extend the electrically encoded THz-TDS system from broadband structural imaging to spectral-fingerprint-based material discrimination with a single detector.

3. Time-of-flight THz three-dimensional and dynamic imaging

3.1. Depth-resolved imaging in transmission geometry

Beyond frequency-resolved reconstruction, the waveform-preserving acquisition also retains the temporal information required for time-of-flight imaging. Because a complete THz electric-field waveform is recorded for each spatial mask, images can be reconstructed not only at selected frequencies, but also at selected temporal delays. These temporal slices correspond to different optical path lengths and therefore provide access to depth information.

We first demonstrated this capability in transmission geometry. Figure 5a shows a representative THz waveform containing temporally separated responses from the air window and two polylactic acid (PLA) regions, while Figure 5b illustrates the corresponding sample geometry. The sample contains an open air window and PLA regions with thicknesses of 1 mm and 2 mm, denoted as Plane1 and Plane2, respectively. By extracting the signals at selected delays, the air window and the two PLA planes were independently reconstructed, as shown in Figure 5c. The separated temporal slices

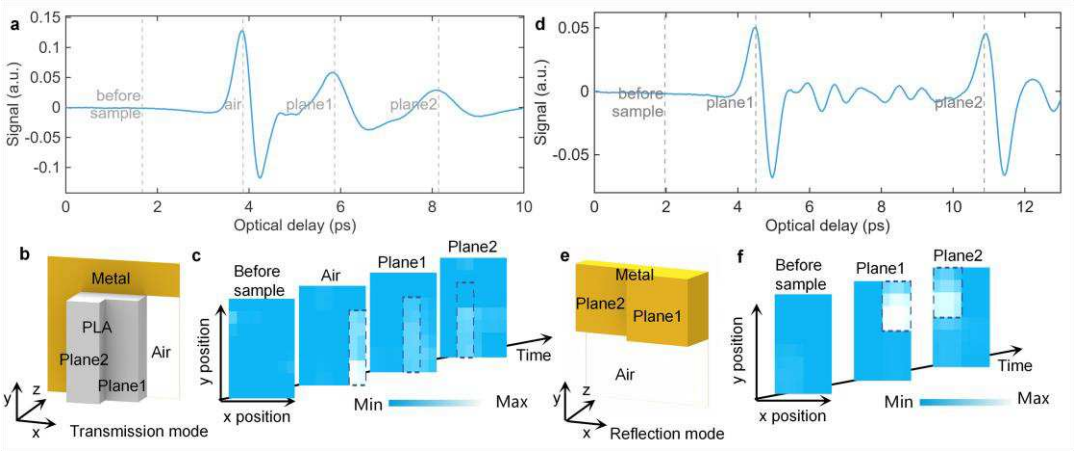


Figure 5. Time-of-flight-based depth-resolved THz single-pixel imaging in transmission and reflection geometries. a, Representative transmission-mode THz waveform, in which different temporal features correspond to the region before the sample, the air window, Plane1, and Plane2. **b,** Schematic of the transmission-mode sample geometry. The sample consists of metal, polylactic acid (PLA), and air regions, where Plane1 and Plane2 correspond to 1 mm and 2 mm thick PLA regions, respectively. **c,** Transmission-mode depth-resolved images reconstructed from selected temporal delays, corresponding to the regions before the sample, the air window, Plane1, and Plane2. **d,** Representative reflection-mode THz waveform, showing temporally separated echoes from Plane1 and Plane2. **e,** Schematic of the reflection-mode sample geometry. The metallic sample contains two reflecting planes, where Plane1 and Plane2 correspond to 1 mm and 2 mm thick metal regions, respectively. **f,** Reflection-mode depth-resolved images reconstructed from selected temporal delays, corresponding to the regions before the sample, Plane1, and Plane2.

confirm that the electrically encoded THz-SLM preserves the waveform information required for transmission-mode depth discrimination.

The reconstructed delays were further compared with the designed PLA thicknesses. Taking the refractive index of 3D-printed PLA[22] as $n_{PLA} = 1.60$, the additional propagation delay is given by $\Delta t = (n_{PLA} - 1)d/c$, where d is the sample thickness and c is the speed of light in air. The designed 1 mm and 2 mm regions therefore correspond to delays of approximately 2.0 ps and 4.0 ps. Experimentally, delays of 2.00 ps and 4.27 ps were obtained, yielding estimated thicknesses of 1.00 mm and 2.13 mm, respectively. The agreement with the designed values confirms the quantitative depth-reconstruction capability of the transmission system, within uncertainties arising from material dispersion, printing tolerance, and variations in the effective refractive index of the fabricated PLA.

3.2. Extension to reflection-mode depth discrimination

Having established transmission-mode depth reconstruction, we next extended the method to reflection geometry for opaque or highly absorbing samples, thereby broadening its applicability to nondestructive testing and biomedical imaging. Figure 5d shows the reflected THz waveform from a metallic step target, and Figure 5e illustrates its two reflecting planes. Plane1 and Plane2 correspond to metal regions with thicknesses of 1 mm and 2 mm, giving a designed height difference of 1 mm. In this geometry, the incident THz pulse is first reflected by the sample, after which the returning field is spatially encoded by the SLM and detected by the single detector, as detailed in Supplementary Fig. S12. This receive-side encoding preserves the same single-pixel measurement principle while avoiding pre-sample insertion loss, temporal echoes, and waveform perturbations from the SLM. The resulting reflected waveform is therefore well suited to time-of-flight analysis. Depth-resolved images reconstructed at the two reflection peaks are shown in Figure 5f. The measured temporal separation is approximately 6.4 ps, corresponding to an optical path difference of 1.92 mm in air. Because reflection involves a double-pass path, the physical height difference is approximately 0.96 mm, in close agreement with the designed 1 mm step. This agreement verifies the quantitative depth-resolving capability of the system in reflection mode.

3.3. Dynamic THz single-pixel imaging

Finally, we applied the same electrically encoded framework to dynamic imaging. As shown in Figure 6, a metallic plate containing a cross-shaped air aperture was translated along the y direction between successive acquisitions. For each frame, 60

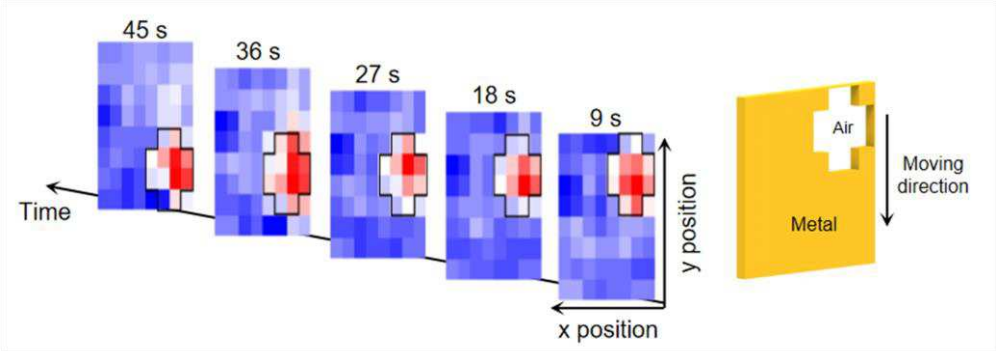


Figure 6. Dynamic THz single-pixel imaging of a laterally moving metallic aperture. Time-sequential reconstructed THz images at 9 s, 18 s, 27 s, 36 s, and 45 s show the motion of a metallic target with a cross-shaped air aperture. The target moves along the y direction, and the corresponding THz images record the dynamic displacement of the aperture in the *x*–*y* plane.

Diag-ordered binary masks were displayed with a dwell time of 80 ms per mask, corresponding to 30 differential Hadamard coefficients and a sampling ratio of 46.8%.

The reconstructed frames at 9, 18, 27, 36, and 45 s capture the progressive displacement of the aperture in the *x*–*y* plane, demonstrating dynamic tracking with electrically programmable spatial encoding (see Supplementary Movie). The approximately 9 s frame-acquisition time represents the present system-level performance rather than the intrinsic response limit of the SLM, as it is mainly determined by lock-in detection, control electronics, and the number of projected masks. These results extend the waveform-preserving platform from static hyperspectral and depth-resolved reconstruction to dynamic THz single-pixel imaging.

Discussion

1. Waveform-preserving THz spatial encoding

Multidimensional THz imaging increasingly requires spatial, spectral, and depth information to be acquired within a unified and compact architecture. Recent broadband THz-SLMs have extended electrically controlled spatial modulation to 0.2-1.0 THz[13]. Nevertheless, the integration of material-specific hyperspectral spectral-fingerprint

imaging and time-of-flight three-dimensional reconstruction within the same electrically programmable THz-TDS framework remains underexplored. Achieving this combination requires a spatial encoder that operates over a broad continuous bandwidth while preserving the coherent temporal waveform of each THz pulse.

This work establishes an electrically programmable ultrawideband THz spatial encoding platform compatible with coherent THz-TDS. Its key contribution is not merely the electrical modulation of THz signal, but the use of this modulation for spatial encoding while preserving the complete temporal electric-field waveform for every mask. This waveform-preserving capability allows a single-detector framework to support frequency-resolved imaging, spectral-fingerprint discrimination, time-of-flight depth reconstruction, and dynamic imaging.

This capability arises from the combined electrical and electromagnetic design of the GaAs Schottky microslit SLM. Reverse-bias-induced carrier depletion controls the free-carrier absorption in *n*-GaAs, while the subwavelength microslits enhance the interaction between the confined THz field and the electrically tunable carrier region. In the present transmission- and reflection-mode imaging configurations, the SLM therefore functions as a broadband amplitude encoder, whereas the spectral phase and depth information are preserved by coherent THz-TDS detection rather than actively modulated by the device. This operating mode should be distinguished from the phase-modulation capability of the same platform. When integrated with a high-resistivity silicon prism in a conductive-interface total-internal-reflection (TIR) geometry, the bias-dependent sheet conductivity can electrically tune the reflected THz phase, as demonstrated in our previous work[23]. The corresponding data in Supplementary Section 9 suggest that this phase-control configuration may provide a route toward electrically programmable THz beam steering and phased-array imaging.

2. Multidimensional imaging and Diag reconstruction

The waveform-preserving operation is directly reflected in the imaging results. In hyperspectral imaging, the reconstructed contrast follows the material-dependent THz spectra rather than only the sample geometry, enabling spectral-fingerprint discrimination relevant to pharmaceutical analysis, chemical identification, and quality inspection. In time-of-flight imaging, temporal slices resolve different optical path lengths in transmission and separated interfaces in reflection. Together, these results show that the SLM acts as a waveform-preserving spatial encoder rather than an

intensity-only mask, which is particularly valuable for multilayer inspection and opaque-sample analysis.

The Diag-ordered Hadamard strategy complements this hardware platform by addressing practical limitations in THz single-pixel imaging. Nonuniform illumination and reduced post-sample signal-to-noise ratio make high-sequency measurements especially vulnerable to noise. By sampling the two-dimensional sequency domain along progressively expanding diagonal paths, Diag provides a balanced low-to-high sequency progression while remaining deterministic and computationally scalable. This sampling strategy supports stable reconstruction without requiring prior knowledge of the target.

3. Performance outlook and application potential

The present dynamic imaging result demonstrates system feasibility rather than the intrinsic speed limit of the SLM. Higher-speed acquisition may be achieved through synchronized electronics, rapid-scan THz-TDS, higher-SNR sources, continuous-wave operation, and adaptive sampling. Further improvements in modulation depth and spatial resolution may also be obtained through finer microslit geometries, double-sided or cascaded Schottky structures, improved fabrication uniformity, and pixel scaling.

Overall, this work integrates compressed spatial acquisition, spectroscopic material discrimination, and time-of-flight depth reconstruction within a compact single-detector architecture. By combining a non-resonant electrically controlled GaAs Schottky microslit SLM, coherent THz-TDS waveform acquisition, and Diag-ordered Hadamard sampling, the platform emphasizes multidimensional information recovery across a broad THz bandwidth. This capability has the potential for nondestructive testing, pharmaceutical analysis, chemical identification, biomedical diagnostics, security screening, and multilayer structure inspection, where spatial, spectral, and depth information are jointly required.

Materials and methods

Device fabrication and assembly

A 0.62 μm thick *n*-GaAs (dopant: Si) layer with a free carrier density of 2×10^{17} cm^{-3} (as measured by Accent ECVpro) was grown by molecular beam epitaxy (MBE) on a 3-inch semi-insulating GaAs substrate (supplied by AXT, Inc.). The "U"-shaped Ohmic contact was fabricated through electron-beam evaporation, sequentially

depositing layers of 20 nm germanium, 20 nm gold, 20 nm nickel, and 200 nm gold, followed by rapid thermal annealing at 400 ℃ for 1 minute. Subsequently, the metal microslits and electrode lines were patterned using conventional photolithography. A 10-nm-thick titanium adhesion layer was first deposited onto the GaAs substrate via electron beam deposition, followed by a 200 nm gold layer, and completed with a lift-off process. Finally, the SLM was electrically integrated by connecting it to a printed circuit board through wire bonding.

Device characterization

Each pixel of the 10 × 10 SLM was independently addressed by one of the 100 output channels of a custom-built MCU. The output voltage was switched between 0 V and −5 V relative to the Ohmic contact, corresponding to the unbiased and 5 V reverse-bias states, respectively. Chessboard patterns and other binary masks were loaded into the MCU to control the transmission state of each pixel. For spatial characterization, the SLM was mounted on a motorized positioning stage, allowing the full modulator area to be raster scanned using a focused THz beam.

Operating configurations

The THz single-pixel imaging system consisted of a commercial THz-TDS system (TERA-K15, Menlo Systems Inc.), the custom-designed SLM, the MCU-based control unit, and two plano-convex lenses with a focal length of 100 mm. For transmission-mode imaging, the THz beam was collimated, spatially encoded by the SLM, transmitted through the sample, and collected by a single photoconductive detector. For reflection-mode imaging, a silicon beam splitter was introduced to direct the reflected THz signal from the sample to the detector. The detailed system configuration for time-of-flight-based depth-resolved THz single-pixel imaging in reflection geometry is illustrated in Fig. S12 of the Supplementary Information.

Data processing

The amplitude-based modulator exhibited binary transmission states, denoted as 1 for the high-transmission state and 0 for the low-transmission state. To emulate the orthogonal ±1 structure of Hadamard matrices, each Hadamard pattern was implemented by sequentially displaying a binary mask and its complementary inverse mask. The measured responses from the complementary pattern pair, corresponding to [1, 0] and [0, 1] states, were subtracted to obtain one differential Hadamard coefficient. Therefore, reconstructing an N-pixel image from M Hadamard coefficients requires $2M$ full time-domain THz waveforms, where $M \leq N$.

For frequency-resolved imaging, each recorded time-domain waveform was Fourier transformed, and the amplitude at the selected THz frequency was extracted. Differential measurements were then obtained by subtracting the Fourier-domain amplitudes of each complementary pattern pair. For time-of-flight depth-resolved imaging, the temporal signal at selected optical delays was directly extracted from each waveform, followed by the same complementary subtraction process. The resulting differential measurement vector at each selected frequency or temporal delay was used for image reconstruction with the TVAL3 algorithm.

Data Availability Statement

The authors confirm that the data supporting the findings of this study are available within the article and its supplementary materials.

Acknowledgements

This work was supported in part by the National Natural Science Foundation of China (Grant Numbers U2330114, 62575188, T2421003, 62575187); the Shenzhen Natural Science Foundation General Project (Grant Numbers JCYJ20230808105907015, JCYJ20240813141411015); the Natural Science Foundation of Guangdong Province (Grant Numbers 2025A1515011392, 2026A1515011664); Medical-Engineering Interdisciplinary Research Foundation of Shenzhen University and the Shenzhen University 2035 Plan Project; Shenzhen Key Laboratory of Photonics and Biophotonics (ZDSYS20210623092006020) and Biomedical Optics Micro-Nano Detection and Imaging (ZDSY20130329101226215).

Conflict of interest

The authors declare that they have no conflict of interest.

References

1 Stantchev, R. I. *et al.* Noninvasive, near-field terahertz imaging of hidden objects using a single-pixel detector. *Sci. Adv.* **2**, e1600190 (2016). https://doi.org/10.1126/sciadv.1600190

2 Cui, Y. *et al.* Hidden-information extraction from layered structures through terahertz imaging down to ultralow SNR. *Sci. Adv.* **9**, eadg8435 (2023). https://doi.org/10.1126/sciadv.adg8435

3 Jiang, X. *et al.* Detection and imaging of chemicals and hidden explosives using terahertz time-domain spectroscopy and deep learning. *Light Sci. Appl.* **15**, 80 (2026). https://doi.org/10.1038/s41377-026-02190-z

4 Fan, F., Ou, Y., Deng, H., Liu, X. & Sun, Y. Advanced spectroscopic techniques for lactose crystallization analysis: investigating water participation in crystal morphology. *Anal. Chem.* **97**, 20688–20697 (2025). https://doi.org/10.1021/acs.analchem.5c00297

5 Leung, C. K., Brauns, H., Ward-Berry, J. N., Finke, J. H. & Zeitler, J. A. Determination of compartment properties of press-coated tablets by non-destructive terahertz technology. *Int. J. Pharm.* **701**, 127081 (2026). https://doi.org/10.1016/j.ijpharm.2026.127081

6 Mou, S. *et al.* All-fibre-coupled terahertz single-pixel imaging for biomedical applications. *Nat. Commun.* **17**, 1571 (2026). https://doi.org/10.1038/s41467-026-68290-x

7 Zhang, X. *et al.* Time-Domain-Filtered terahertz nanoscopy of intrinsic light–matter interactions. *Nano Lett.* **24**, 15008–15015 (2024). https://doi.org/10.1021/acs.nanolett.4c03715

8 Li, X. *et al.* Plasmonic photoconductive terahertz focal-plane array with pixel super-resolution. *Nat. Photon.* **18**, 139–148 (2024). https://doi.org/10.1038/s41566-023-01346-2

9 Baraniuk, R. G. Compressive sensing. *IEEE Signal Process. Mag.* **24**, 118–121 (2007). https://doi.org/10.1109/MSP.2007.4286571

10 Stantchev, R. I., Yu, X., Blu, T. & Pickwell-MacPherson, E. Real-time terahertz imaging with a single-pixel detector. *Nat. Commun.* **11**, 2535 (2020). https://doi.org/10.1038/s41467-020-16370-x

11 Malevich, Y., Ergoktas, M. S., Bakan, G., Steiner, P. & Kocabas, C. Very-large-scale reconfigurable intelligent surfaces for dynamic control of terahertz and millimeter waves. *Nat. Commun.* **16**, 2907 (2025). https://doi.org/10.1038/s41467-025-58256-w

12 Zhu, W. *et al.* High-contrast transmissive terahertz programmable metasurface based on liquid crystal. *ACS Photonics* **12**, 3892–3900 (2025). https://doi.org/10.1021/acsphotonics.5c00938

13 Liu, C. *et al.* Broadband terahertz liquid crystal spatial light modulators for multispectral single-pixel imaging and beam scanning. *ACS Photonics* **13**, 2687–2695 (2026). https://doi.org/10.1021/acsphotonics.6c00283

14 Liu, X., Chen, X., Parrott, E. P. J. & Pickwell-MacPherson, E. Exploiting a metal wire grating in total internal reflection geometry to achieve achromatic polarization conversion. *Photonics Res.* **5**, 299–304 (2017). https://doi.org/10.1364/PRJ.5.000299

15 Liu, X. *et al.* Ultrabroadband electrically controllable terahertz modulation based on GaAs Schottky diode structure. *APL Photonics* **6**, 111301 (2021). https://doi.org/10.1063/5.0064643

16 Huggard, P. G. *et al.* Drude conductivity of highly doped GaAs at terahertz frequencies. *J. Appl. Phys.* **87**, 2382–2385 (2000). https://doi.org/10.1063/1.372238

17 Vaz, P. G., Amaral, D., Requicha Ferreira, L. F., Morgado, M. & Cardoso, J. Image quality of compressive single-pixel imaging using different Hadamard orderings. *Opt. Express* **28**, 11666–11681 (2020). https://doi.org/10.1364/OE.387612

18 Yu, W. K. Super sub-Nyquist single-pixel imaging by means of cake-cutting Hadamard basis sort. *Sensors* **19,** 4122 (2019). https://doi.org/10.3390/s19194122

19 Li, C., Yin, W., Jiang, H. & Zhang, Y. An efficient augmented Lagrangian method with applications to total variation minimization. *Comput. Optim. Appl.* **56**, 507–530 (2013). https://doi.org/10.1007/s10589-013-9576-1

20 Datta, S. *et al.* Terahertz spectroscopic analysis of lactose in infant formula: implications for detection and quantification. *Molecules* **27,** 5040 (2022). https://doi.org/10.3390/molecules27155040

21 D'Angelo, F., Mics, Z., Bonn, M. & Turchinovich, D. Ultra-broadband THz time-domain spectroscopy of common polymers using THz air photonics. *Opt. Express* **22**, 12475–12485 (2014). https://doi.org/10.1364/OE.22.012475

22 Freitas, G. F., Roque, L. T., Kawahala, N. M. & Hernandez, F. G. G. Optical analysis of 3D-printed terahertz waveplates from common thermoplastics. *Sci. Rep.* **16**, 2532 (2026). https://doi.org/10.1038/s41598-025-32267-5

23 Liu, X. et al. Broadband terahertz phase modulation using a GaAs Schottky diode with integrated subwavelength metal microslits in total internal reflection geometry. J. Lightwave Technol. 43, 8254-8262 (2025). https://doi.org/10.1109/JLT.2025.3581318

Supplementary Files

This is a list of supplementary files associated with this preprint. Click to download.

- DynamicTHzsinglepixelimagingofalaterallymovingmetallicaperture.mp4
- SI.pdf